Three-Dimensional FDTD Simulation of Micro-Pillar Microcavity Geometries Suitable for Efficient Single-Photon Sources

Ying-Lung Daniel Ho, Tun Cao, Pavel S. Ivanov, Martin J. Cryan, Ian J. Craddock, Chris J. Railton, and John G. Rarity

***Abstract*—We present the results of calculations of the microcavity mode structure of distributed-Bragg-reflector (DBR) micro-pillar microcavities of group III–V semiconductor materials. These structures are suitable for making single photon sources when a single quantum dot is located at the center of a wavelength scale cavity. The 3-D finite difference time domain (FDTD) method is our primary simulation tool and results are validated against semi-analytic models. We show that high light extraction efficiencies can be achieved ($> 90\%$) limited by sidewall scattering and leakage. Using radial trench DBR microcavities or 2-D photonic crystal structures, we can further suppress sidewall emission, however, light is then redirected into other leaky modes.**

***Index Terms*—Bragg reflection, cavity quantum electrodynamics, light confinement, optical microcavities, photonic bandgaps, quantum dots, spontaneous emission modification.**

I. Introduction

HERE we are interested in wavelength-scale quantum photonic devices made of III–V semiconductor materials. Typically, photons are confined by distributed Bragg reflection and total internal reflection (TIR). These structures show both small effective modal volumes (V_{eff}) and relatively high quality factors (Q) and thus form high Q/V_{eff} cavities. The simplest model takes a Fabry–Perot (FP) cavity containing a dipole source [1]. Owing to the microcavity, the field distribution of photon emission is strongly modified and consists of well-separated modes equally spaced in k-space. When the cavity is also transversely limited, for instance by etching a pillar, the cavity modes are further confined by total internal reflection. For high-refractive-index pillars, we find that a significant fraction of the spontaneous emission will be collected into these cavity modes. The combination of confinement and cavity resonance leads to modifications of the spontaneous emission (SE) rate as first proposed by Purcell [2] in 1946 and further enhances the efficiency of collection into useful modes. Efficient single-photon sources can thus be made by incorporating single self-assembled quantum dots (QDs) resonant with such structures [3]–[6]. Highly efficient single-photon sources are required for photonic quantum information applications, such as quantum communication [7] and quantum computation [8]. This can be investigated using either a classical analysis [9] or quantum analysis [10]. In a classical analysis, we can place a simple dipole source at the center of the cavity and assume that the field in the cavity has no back action effect on the dipole. In the finite-difference time-domain (FDTD) method [11], [12], a short few-cycle pulse is applied to the dipole, and the method calculates the ringdown in the time domain by solving Maxwell's equations by time stepping on a subwavelength grid. This allows the calculation of the spontaneous emission rate, the external quantum efficiency, and the spontaneous emission in a microcavity of arbitrary geometry.

In Section II, we briefly review a semi-analytic method to calculate the fundamental guided modes in pillar microcavities. This method combines a transfer-matrix model (TMM) [13] for the planar cavity with a waveguide mode solution [14], [15] using an effective refractive index in the pillar. In Section III, we then focus on the 3-D FDTD method used for the detailed investigation of design parameters for different types of microcavity geometries. These include circular and square pillars, radial trench distributed-Bragg-reflector (DBR) microcavities [16], and quasi-three-dimensional (quasi-3-D) photonic crystal defect microcavities [17], [18]. These last cavities are designed to further suppress transverse emission and leakage. As a result of these calculations, we are able to propose the optimal design of micro-pillar microcavities suitable for generating single photons on demand. We are also able to compare our calculated enhancements of spontaneous emission rates (Purcell factors) to those obtained from simpler approximations [19].

II. Approximate Model for QDs in Micro-Pillar Microcavity Simulations

The calculation of the interference effects of a system of thin layers can be accomplished by considering a light wave incident on the multilayer structure and reflected forwards and backwards between the various interfaces. In the steady state, the light waves combine to form the transmitted or reflected light

Manuscript received September 3, 2006; revised January 26, 2007. This work was supported in part by the EPSRC IRC in Quantum Information Processing and by the European Commission under the Integrated Project Qubit Applications. The work of J. G. Rarity was supported by the Royal Society through a Wolfson Merit Award.

Y.-L. D. Ho, T. Cao, P. S. Ivanov, M. J. Cryan, and J. G. Rarity are with the Photonics Research Group, Centre for Communications Research (CCR), Department of Electrical and Electronic Engineering, University of Bristol, Bristol, U.K. (e-mail: Daniel.Ho@bris.ac.uk; Tun.Cao@bris.ac.uk; P.Ivanov@bris.ac.uk; M.Cryan@bris.ac.uk; John.Rarity@bris.ac.uk).

I. J. Craddock and C. J. Railton are with the Computational Electromagnetics Group, Centre for Communications Research (CCR), Department of Electrical and Electronic Engineering, University of Bristol, Bristol, U.K. (e-mail: Chris.Railton@bris.ac.uk; Ian.craddock@bristol.ac.uk).

Color versions of one or more of the figures in this paper are available online at http://ieeexplore.ieee.org.

Digital Object Identifier 10.1109/JQE.2007.897905

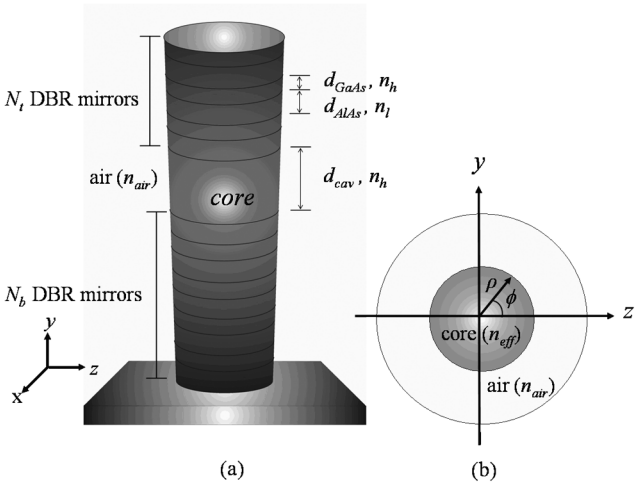

Fig. 1. Schematic representation of cylindrical micro-pillar microcavity. (a) Cylindrical pillar with alternating layers (d_{GaAs} and d_{AlAs}) of high (n_h) and low (n_l) refractive index and central cavity (d_{cav}) containing high-refractive-index material. (b) Cross section of the waveguide model showing a central waveguide with effective refractive index n_{eff} surrounded by air with refractive index $n_{\mathrm{air}} = 1$. (ρ, ϕ) is the cylindrical transverse coordinate system.

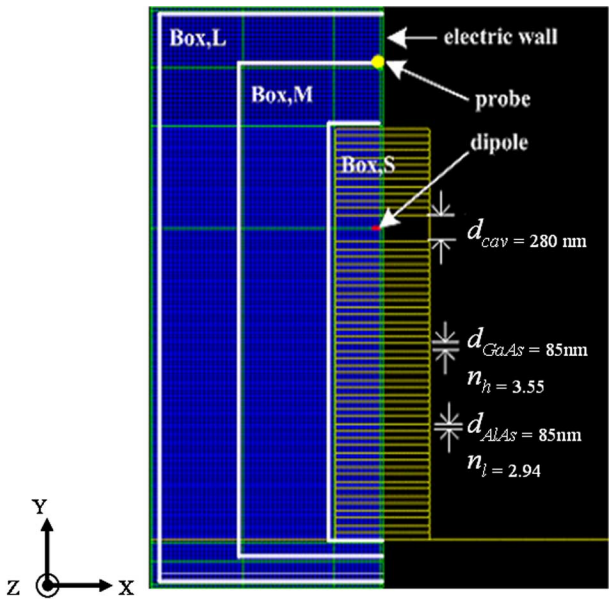

Fig. 2. Y–X plane of device showing the mesh, electric wall, probes, QD broadband dipole, cavity thickness (d_{cav}), and DBR periodicity (d_{AlAs} and d_{GaAs}). Cavity shows six mirror pairs on top and 21 below.

wave. This can be straightforward to implement numerically by means of the TMM [13]. The TMM works well for simple planar cavities with lateral dimension much larger than the wavelength.

To deal with wavelength-scale pillars, a semi-analytic waveguide method can be used [14], [15]. In this method, the pillar is treated as a waveguide with an effective refractive index, n_{eff}. A schematic representation of cylindrical micro-pillar microcavity is shown in Fig. 1. The structure includes a microcavity region with a high-refractive-index (n_h) layer of thickness d_{cav} sandwiched between two dielectric mirrors made by a high-refractive-index (n_h) layer of thickness d_{GaAs} and a low-refractive-index (n_l) layer of thickness d_{AlAs}. In addition, at the center of the microcavity region, there is a layer of QDs resonant with the cavity at an antinode of the field. The cavity resonant condition is then satisfied when

$$\beta \cdot d_{\mathrm{cav}} = 2\pi \tag{1}$$

where $\beta = ((2\pi \cdot n_{\mathrm{eff}} \cdot \cos\Theta)/\lambda)$ is the component of the wavevector along the pillar, where λ is the cavity-resonant wavelength, where $\Theta = \sin^{-1}(h/(k_0 n_{\mathrm{eff}}))$, and where h is the transverse wavevector in the pillar.

As the pillar diameter shrinks, β is reduced and the resonance blue-shifts. We have implemented this approximation as it is described in [15] and use it to validate our FDTD results.

III. 3-D Model for QDs in Micro-Pillar Microcavity Simulations

We used the FDTD method based on the model proposed by Yee [21], which has been widely used in microwave engineering. In recent years with the advent of high-performance desktop and low-cost random access memory (RAM), the FDTD method has been widely applied in the optics regime [11]. In this section, we use the University of Bristol in-house code, which has been developed over a number of years, to calculate the optical characteristics of these structures.

A. Different Types of Microcavity Geometries

For the FDTD simulation, we build a grid model of the pillar microcavity using refractive indexes as described above; the graphical user interface (GUI) output for the model is shown in Fig. 2. The microcavity consists of a GaAs λ-cavity ($d_{\mathrm{cav}} = \lambda_r/n_h$) surrounded above and below by DBR mirrors. Below there are N_b pairs of alternating GaAs–AlAs quarter-wave layers ($d_{\mathrm{GaAs}} = \lambda_r/(4n_h)$ and $d_{\mathrm{AlAs}} = \lambda_r/(4n_l)$) and above N_t pairs with $n_h = 3.55$ and $n_l = 2.94$. The grid size in the high-refractive-index region is 23.33 nm, while in the lower refractive index region it is 28.33 nm. The design resonant wavelength is $\lambda_r = 994$ nm.

Typically, for high-efficiency vertical photon emission, the number of mirror pairs in the bottom DBR is larger than the number above $N_b > N_t$. Here, we place a broadband dipole source in the center of the GaAs cavity to probe the guided fundamental HE_{11} mode. As the structures which we are designing are all symmetrical about the Z–Y plane, we can speed up the simulation by introducing an electric wall in this plane (see Fig. 2). However, the FDTD technique allows us to go beyond simple circular symmetric pillars. In this paper, we consider more sophisticated structures based on circular and square radial trench DBRs [16], and triangular and square lattice quasi-3-D photonic crystal defect microcavities [17], [18]. The motivation for putting such structures in the X–Z plane is to suppress sidewall leakage (see Fig. 3) and thus increase light collection into the vertical emitting modes.

Thus, the initial design of the lateral Bragg reflectors is to make the air trench and solid region thickness $\lambda_r/(4n)$, where the refractive index $n = n_{\mathrm{eff}} = 3.33$ [20] in the solid section

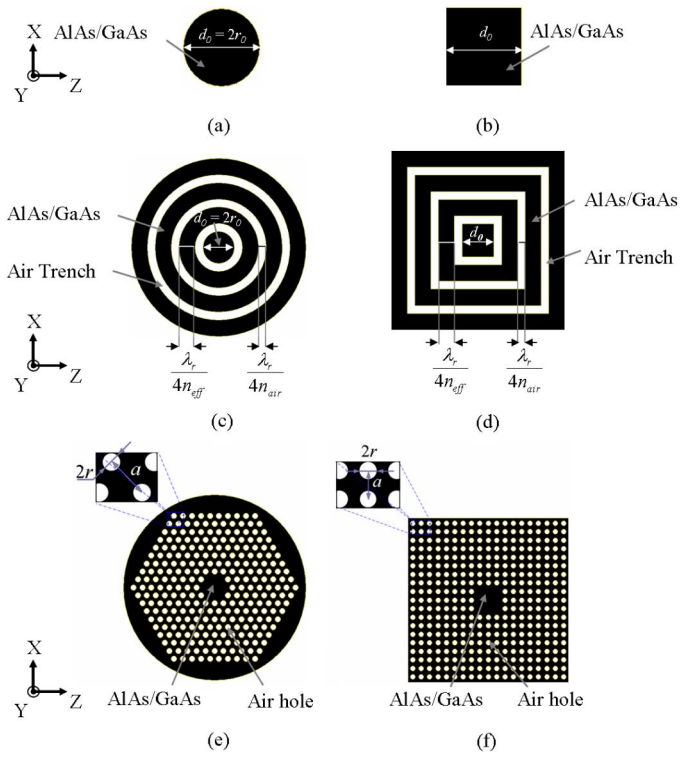

Fig. 3. (a)–(f) Top views of the circular and square pillar microcavities, the circular and square radial trench DBR microcavity pillars, and the square lattice and triangular lattice quasi-3-D photonic crystal defect microcavity pillars with single QD emitter sitting in the center of cavity. Black areas represent GaAs–AlAs and white areas air trenches/holes. (a) Diameter of the circular pillar is d_0 and (b) the side-length of a square pillar cavity is d_0. The thickness of radial DBRs are $\lambda_r/(4n_{\text{eff}}) = 0.525\ \mu$m and $\lambda_r/(4n_{\text{air}}) = 0.25\ \mu$m at the resonant wavelength of $\lambda_r = 994$ nm. Pitch a and radius r of the regular air holes are $a = 0.2\ \mu$m and $r = 0.066\ \mu$m in (c) and $a = 0.188\ \mu$m and $r = 0.0623\ \mu$m in (d) at the resonant wavelength of $\lambda_{\text{res}} = 994$ nm.

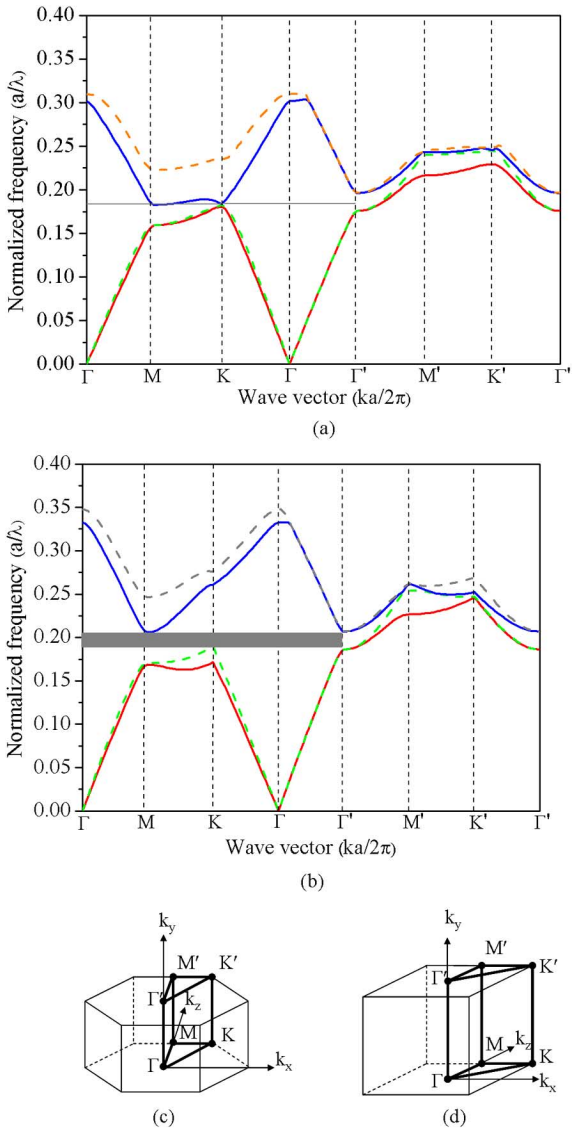

Fig. 4. Quasi 3-D photonic crystal band diagrams calculated using the MPB [22] package. Vertical structure is an infinite DBR while the lateral structure is a periodic hole array with radius to pitch ratio $r/a = 0.33$. Band diagrams plotting allowed frequencies against wave-vectors of the triangular lattice are shown in (a) following the points Γ–M–K–Γ–Γ'–M'–K'–Γ' on (c) the Brillouin zone. For the square lattice, (b) shows the band diagram following the same route on (d) the Brillouin zone. In the band diagrams, the lines correspond to propagating (Bloch) modes and the gray regions show the bandgaps where no propagating modes exist. We note that only a narrow bandgap exists for the triangular lattice that widens for the square lattice. For $\lambda_r = 994$ nm $a = 0.2\ \mu$m guarantees no propagation through the triangular lattice while for the case of the square lattice $a = 0.188\ \mu$m.

and in air $n = n_{\text{air}} = 1$ as shown in Fig. 3(c) and (d). To design the quasi-3-D photonic crystal, it was necessary to have an initial idea of structures that would block horizontal emission. Thus, we used the plane-wave expansion (PWE) method to calculate band diagrams for infinite structures. The FDTD method could in principle be used to do this, however, the required periodic boundary conditions are not implemented in our code. Here the MIT photonic-bands (MPB) PWE package [22] was used to give a full-vectorial calculation of band diagrams of an infinite DBR structure containing periodic vertical holes. The results are shown in Fig. 4(a) and (b), while the Brillouin zone for triangular lattice and square lattice are shown in Fig. 4(c) and (d), respectively. We see that bandgaps do exist for propagation in the X-Z plane (Γ-M-K-Γ) and for propagation in the Y direction (Γ'). We note that the bandgap for the triangular lattice is very narrow. However, between the X-Z plane and the Y-direction (Γ'-M'-K'-Γ'), propagating modes exist. A complete photonic bandgap in 3-D is not expected due to the angular dependence of the 1-D and 2-D gaps and the anisotropy of the Brillouin zone [17]. However, we clearly show the overlap of 2-D and 1-D gaps at Γ' and hope then to suppress side emission. For $\lambda_r = 994$ nm and the DBR parameters described above, a photonic crystal period $a = 0.2\ \mu$m guarantees no propagation through the triangular lattice while for the case of the square lattice $a = 0.188\ \mu$m (hole radius to period ratio is 0.33 in both cases). Having done an approximate design of the photonic crystal, we are then able to build the grid model, including the cavity and vertical guiding defect, and calculate the full electromagnetic fields using the 3-D FDTD method.

B. Mode Spectrum of Microcavity Geometries

In order to obtain the mode spectra, we place a broadband dipole source in the center of the microcavity and input a short few-cycle excitation pulse. The cavity then rings at its resonant

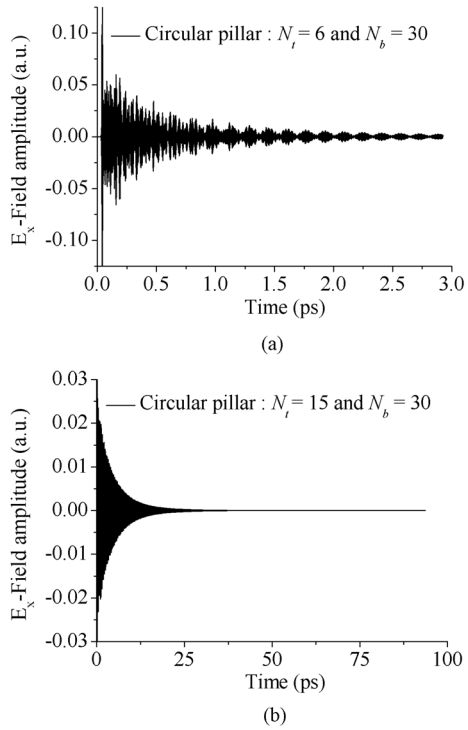

Fig. 5. Probed E_x-field amplitude as a function of time for the $d = 1.05$ μm circular pillar. (a) Low–Q cavity with $N_t = 6$ top mirror pairs and $N_b = 30$ bottom pairs. (b) High-Q cavity with $N_t = 15$ top mirror pairs and $N_b = 30$ bottom pairs.

frequency, and we monitor the cavity ringdown in the time domain using a probe placed above the pillar. The number of time steps is chosen such that the ringdown signal has fully decayed by the end of the simulation. Waiting several exponential decay times ensures accurate estimates of Q-factor (see the following). In high-Q cavities, up to one million time steps were used.

We show the ringdown for typical microcavity geometries in Fig. 5. Fig. 5(a) shows ringdown for a typical low-Q cavity with $N_t = 6$ top mirror pairs and $N_b = 30$ bottom pairs and Fig. 5(b) shows ringdown for a typical high-Q cavity with $N_t = 15$ top mirror pairs and $N_b = 30$ bottom pairs. Taking the Fourier transform of the ringdown signal allows us to determine the resonant frequencies of the waveguide cavity as shown in Fig. 6(a) and (b). We fit the spectral data to a Lorentzian model

$$S(\lambda) = \frac{1}{\pi} \frac{A\Delta\lambda_r}{(\Delta\lambda_r)^2 + 4(\lambda - \lambda_r)^2} + B \tag{2}$$

where λ_r is the resonant wavelength, $\Delta\lambda_r$ is the peak full-width at half-maximum (FWHM) and peak area A and background level B are fitting constants. We have calculated resonant wavelength λ_r and Q-factors of various pillar dimensions for circular and square micro-pillar microcavities, radial trench DBR microcavity pillars, and quasi-3-D photonic crystal defect microcavity pillars as shown in Fig. 6. The results in Fig. 7 show that the cavity mode blue-shifts to higher energy or shorter wavelength as diameter decreases in reasonable agreement with the waveguide method (Section II). The transfer matrix model (TMM) result shows a resonance at 994 nm corresponding to the resonance in an infinite planar cavity. However, the FDTD calculation shows a systematic wavelength shift from the waveguide method (and the TMM result) of about 1.8%. We ascribe this to a gridding error and have done a convergence check using smaller grid size as shown in the inset of Fig. 7. Normally, FDTD calculations require the maximum cell size in high field regions to be less than $\lambda_{\min}/15$, where $\lambda_{\min}$ is the smallest guided wavelength corresponding to the upper bandwidth of excitation [11]. However, we see here that this is not adequate for accurate determination of the position of narrow resonances to better than 1%. However, this also gives us an indication that the systematic gridding error we may be seeing in other parameters will also be less than 2%. When we take the gridding error into account, we see that the semi-analytic waveguide and FDTD method blue-shift diverges at small pillar diameters. We ascribe this to the breakdown of the semi-analytic waveguide method for small pillar diameter.

We present the variation of Q-factor with microcavity lateral dimension showing high-Q cavity and low-Q cavity results in Fig. 8. For high-Q cavities of large diameter of pillars ($d > 2$ μm), the Q-factor of 10 000 is close to that of a planar cavity. When the diameter of the pillar is less than 1.5 μm, the Q-factor drops. In simple terms, we know that the reflectivity of the mirror will reduce as the diameter decreases as more and more of the field will lie outside the mirror, and of course at zero diameter the Q-factor is necessarily zero. However, more analytic studies [23] show that scattering into other modes will occur due to the strong transverse-mode component mismatch between the GaAs spacer-layer cavity HE_{11} mode and the corresponding fundamental DBR mirror pairs GaAs–AlGaAs Bloch mode field. This analytic study also shows quite complex behavior due to the subtle transverse resonances which may account for the fluctuations we see in Q-factors below $d = 1$ μm. Other studies also place upper limits on the Q-factor due to inherent scattering at the interstices between air/GaAs–AlGaAs [24]. For low Q-factor cavities, we see little or no reduction of Q-factor with radius.

C. Electric Field Amplitude Distribution of the Fundamental Cavity Mode

Having determined the resonant frequency, we can visualize the electric field on-resonance using a single-frequency "snapshot." We illustrate the lateral confinement of the electric field amplitude distribution of the fundamental cavity mode in circular and square micro-pillar microcavities on resonance in Fig. 9. We clearly see strong emission from the top of the cavity and a small amount of sidewall leakage. Traveling down through the lower Bragg reflector, the fundamental mode disappears and a more complex higher order mode appears to form. This is clear evidence of the scattering process that occurs at the air–GaAs–AlGaAs intersections [24] inducing mode coupling between the fundamental and higher order modes. The mirror is less reflective for these modes, and thus they propagate further and dominate the field picture in the lower part of the pillar. It is this process that reduces the Q-factor for smaller pillar diameters. In Fig. 10, we show the field distribution in circular and

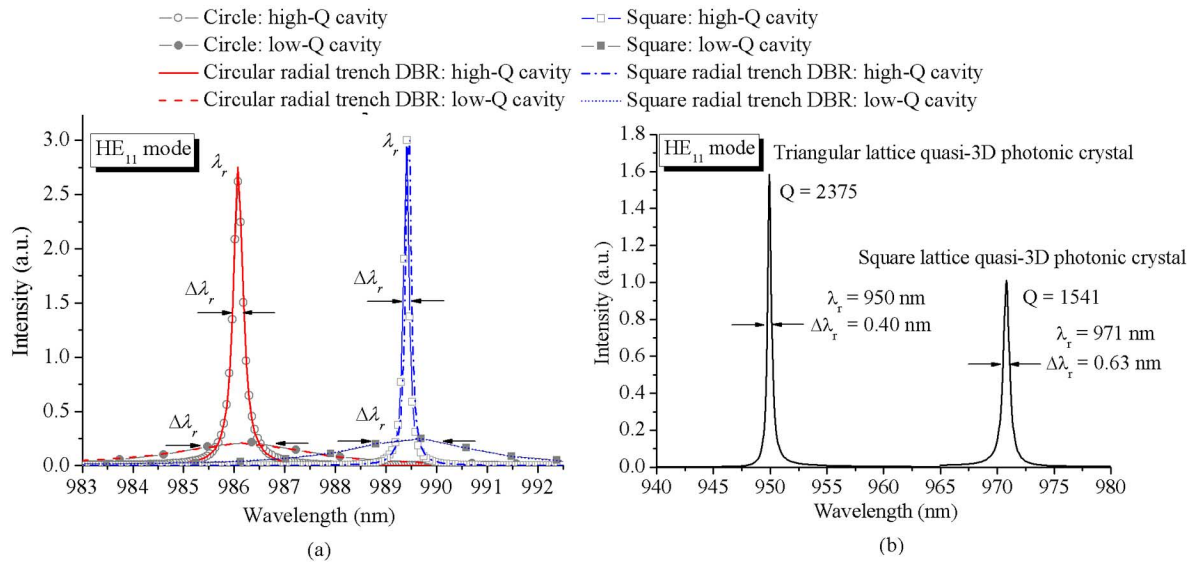

Fig. 6. (a) Mode spectra of the $d = 1.05\ \mu$m circular pillar microcavities (high-Q cavity: $\lambda_r = 986.07$ nm, $\Delta\lambda_r = 0.24$ nm, $Q = 4108$; low-Q cavity: $\lambda_r = 986.07$ nm, $\Delta\lambda_r = 2.95$ nm, $Q = 334$) and square pillar microcavities (high-Q cavity: $\lambda_r = 989.41$ nm, $\Delta\lambda_r = 0.117$ nm, $Q = 8456$; low-Q cavity: $\lambda_r = 989.41$ nm, $\Delta\lambda_r = 2.84$ nm, $Q = 348$) and circular radial trench DBR microcavity pillars (high-Q cavity: $\lambda_r = 986.07$ nm, $\Delta\lambda_r = 0.23$ nm, $Q = 4287$; low-Q cavity: $\lambda_r = 986.07$ nm, $\Delta\lambda_r = 3.06$ nm, $Q = 273$)and square radial trench DBR microcavity pillars (high-Q cavity: $\lambda_r = 989.46$ nm, $\Delta\lambda_r = 0.11$ nm, $Q = 8995$; low-Q cavity: $\lambda_r = 989.46$ nm, $\Delta\lambda_r = 2.80$ nm, $Q = 353$) for low-Q cavity with $N_t = 6$ top mirror pairs and $N_b = 30$ bottom pairs and high-Q cavity with $N_t = 15$ top mirror pairs and $N_b = 30$ bottom pairs. (b) Resonant mode spectra of the triangular and square lattice quasi-3-D photonic crystal defect microcavities with $N_t = 15$ top mirror pairs and $N_b = 30$ bottom pairs.

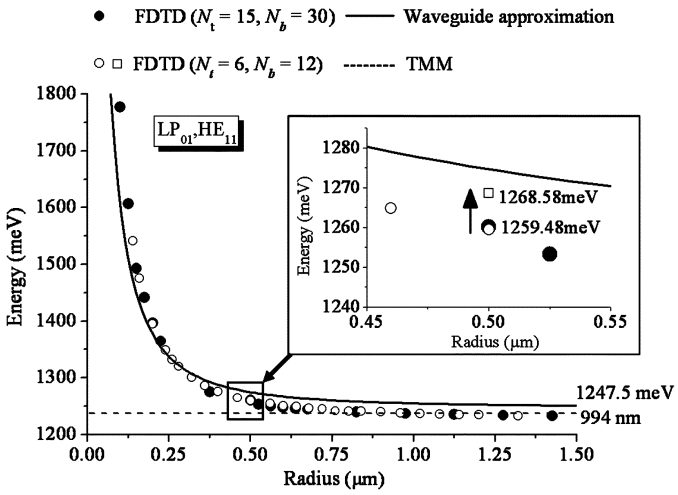

Fig. 7. Comparison of blue-shifts for the lowest energy modes of micro-pillar microcavities calculated by the semi-analytic waveguide method, FDTD, and TMM. The arrow highlights 1.8% absolute error in the resonance determined by FDTD method. We think that this is due to gridding error. By reducing the grid size to $X = 3.33$ nm, $Y = 4.66$ nm, and $Z = 20$ nm, we see in the inset that this shift is reduced (open square) to 1%.

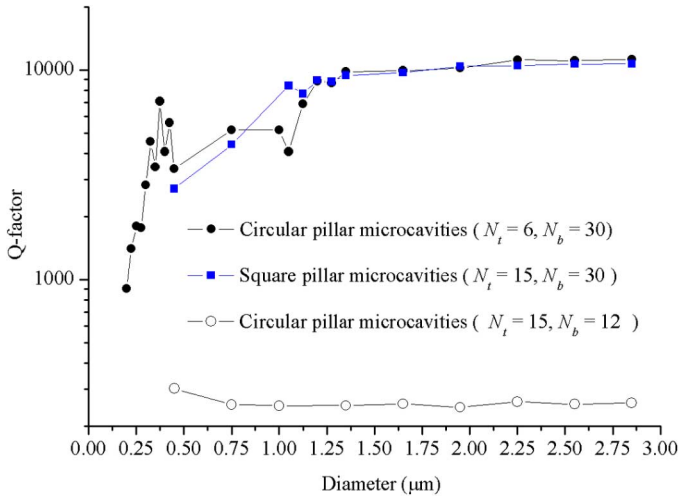

Fig. 8. Q-factors of the fundamental HE_{11} modes of circular and square pillars as a function of diameters calculated by the FDTD method with 15 DBR pairs on top and 30 pairs on bottom, and the structure of six DBR pairs on top and 12 pairs on bottom. Solid circles: circular pillar with 15 DBR pairs on top and 30 pairs on the bottom; solid squares: square pillar with 15 DBR pairs on top and 30 pairs on the bottom; open circles: circular pillar with six DBR pairs on top and 12 pairs on the bottom.

square radial DBR microcavities. The fundamental resonance [as seen in Fig. 6(a)] in the pillar appears largely unchanged. However, the side emission appears suppressed with some evidence of a complex mode structure. In Fig. 11, we visualize the field in quasi-3-D photonic crystal defect microcavities. Lateral emission is again suppressed. However, we see that for the triangular lattice leakage is confined to the Z direction due to the narrow bandgap (see Fig. 4). In the square lattice, we see strong suppression of side emission. The maximum value of the field appears lower in this structure reflecting the lower value of the measured Q-factor [Fig. 6(b)]. One final point to notice is that the emission from below the cavity appears to be similar for all structures.

D. Extraction Efficiency for Micro-Pillar Microcavities

The FDTD code gives the full information on electric and magnetic fields in the defined snapshot planes. Thus, we can calculate the Poynting vector and intensity (I) emitted through planes defined at the sides, top, and bottom of the cavities. This

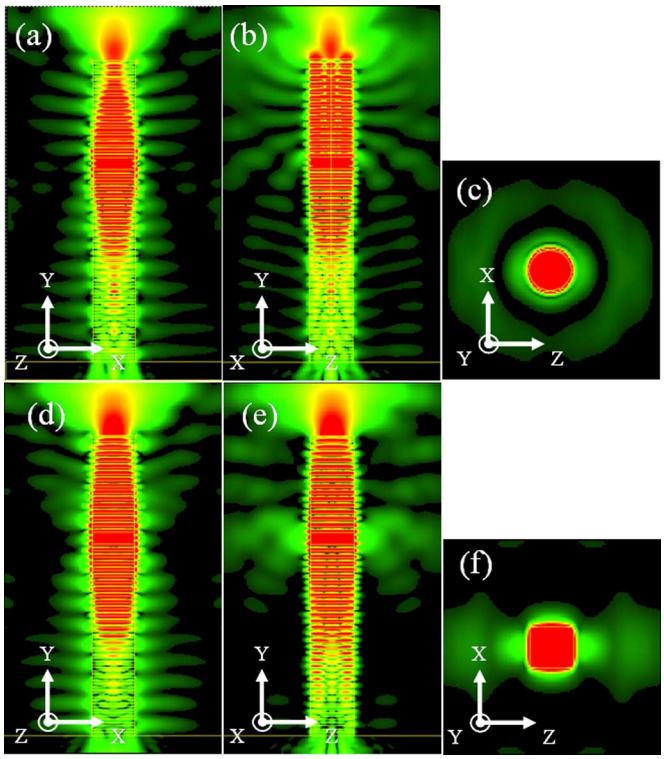

Fig. 9. Resonant frequency snapshot of the E_x-field for the circular pillar microcavity in each plane (a) X-Y, (b) Y-Z, (c) X-Z, and for the square pillar microcavity in each plane (d) X-Y, (e) Y-Z, and (f) X-Z for the fundamental HE_{11} mode. The resonant wavelength is 986.07 nm in the circular microcavity and 989.41 nm in the square microcavity.

then allows us to quantify the efficiency of emission from the top of the cavity and the leakage from sides and bottom of the cavity. To estimate the light extraction efficiency (η), we calculate the total intensity emitted from a box surrounding the microcavity I_{tot} and compare this to the intensity passing through the top X-Z plane I_{top} of the box

$$\eta = \frac{I_{\mathrm{top}}}{I_{\mathrm{tot}}}. \tag{3}$$

The validity of the Poyting vector analysis technique was confirmed by repeating the calculation for various box sizes as indicated in Fig. 2. I_{tot} was found to remain constant to within 0.1% as expected. The efficiency estimates did however vary by $\pm 3\%$. To calculate the efficiencies, we limited ourselves to low-Q cavities with $N_t = 6$ top DBR mirror pairs to minimize the calculation times and allow the various cavity geometries to be tested. Extraction efficiencies for the various microcavity geometries are plotted against the number of periods of DBR bottom mirrors N_b in Fig. 12. In all microcavity geometries, light extraction efficiency increases continuously with the bottom mirror reflectivity. We see that there is only a slight improvement by extending the number of bottom mirror further than 27 pairs. Surprisingly, the simple circular pillars turn out to have the highest efficiency. We see light extraction efficiency of more than 90% when $N_b = 30$. In the radial trench DBR and photonic crystal defect microcavities, the efficiency is below that of the simple circle pillar. We investigate this through studies of side and bottom leakage in Section III-E.

E. Measurement of Leakage in the Various Microcavity Geometries

When the bottom mirror reflectivity is much greater than the top mirror, we expect the efficiency to be limited by light leakage from the sidewalls, which is why we have investigated the structures based on radial trench DBR and photonic crystal defect microcavities. We can trace the sources of leakage simply by looking at the percentage of light lost through side leakage for the different cavity geometries for fixed $N_t = 6$ top mirror pairs and different N_b =12, 15, 18, 21, and 30 bottom pairs as in Fig. 13. We also plot the fraction of intensity leaking through the bottom mirror as a function of increasing numbers of mirror pairs in Fig. 14. For the bare pillars, the sidewall leakage amounts to between 4% and 8% of the total emission. This drops in the circular radial trench geometry (1.5%–4.5%) and further in the square radial trench geometry (1%–1.5%). The triangular lattice photonic crystals have 1.8%–2.2% side leakage and square photonic crystal has the lowest sidewall leakage of 0.4–1%. However, this suppression comes at the price of enhanced bottom leakage. In Fig. 14, we see that the lowest leakage from the bottom of the cavity occurs when the bottom mirror is 30 pairs thick. We immediately see that most of the light that has been blocked from traveling transversely out of the cavity has been redirected into the substrate. This figure is up to 20% in the square lattice photonic crystal while it is as low as 3% in the circular pillar.

F. Optimizing the Design of Micropillar Microcavities

Our experimental samples have slightly different mirror composition, $n_l = 3$ and $n_h = 3.521$ (refer to [25]) and have been designed around $N_b = 27$ mirror pairs. To optimize these samples, we have calculated light extraction efficiencies and Q-factors of 1-μm-diameter circular pillars for a fixed $N_b = 27$ and changing the number of periods of top DBR mirror pairs between $N_t = 6$ and $N_t = 20$). Fig. 15 shows the optimal values of the light extraction efficiency plotted as a function of the number of top DBR pairs, with each curve calculated for a fixed number of periods for the bottom DBR. For the single-photon-source application, we would like not only high efficiency but also a reasonably high Q-factor to maintain a high Purcell factor (see Section III-G). We see that we can achieve $Q > 2500$ with efficient vertical emission $\eta > 70\%$ with $N_t = 14$. When we consider the growth technique constraints, this value is a good tradeoff. Such devices could make efficient single-photon sources for quantum information applications.

G. Estimation of Purcell Factors

As we shrink the radius of the micro-pillar microcavity, the modal volume (V_{eff}) is reduced, which increases the coupling of the dot to the microcavity mode and strongly enhances spontaneous emission. The factor by which the spontaneous emission rate is enhanced is called the Purcell factor (F_p). It can be obtained from Fermi's golden rule with the addition of the local radiative density of states (LRDOS) [26].

Here, we can use the FDTD method to estimate the enhancement in a semiclassical way [9]. The coupling of our dipole into the cavity will be modulated in a similar way to the spontaneous emission by the LRDOS. Hence, the ratio of total emission from

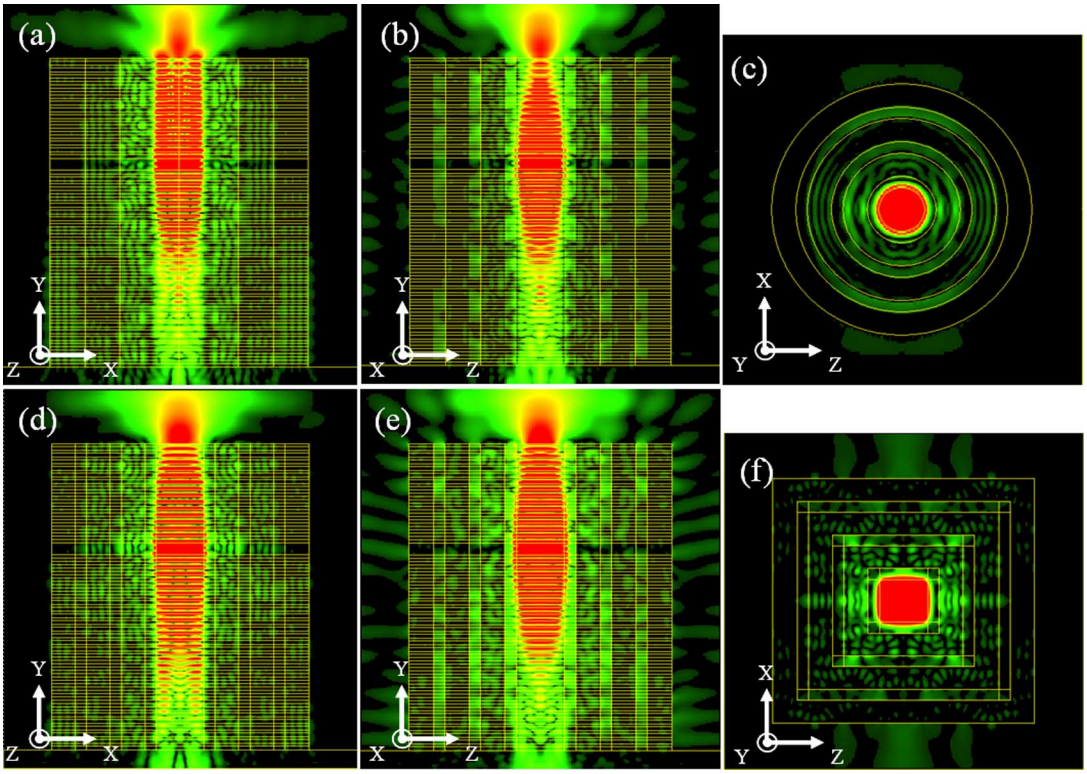

Fig. 10. Resonant frequency snapshot of the E_x-field for the circular radial trench DBR microcavity pillar in each plane (a) X-Y, (b) Y-Z, (c) X-Z and for the square radial trench DBR microcavity pillar in each plane (d) X-Y, (e) Y-Z, and (f) X-Z for the fundamental HE_{11} mode. The resonant wavelength is 986.07 nm in the circular radial trench DBR microcavity and 989.46 nm in the square radial trench DBR microcavity.

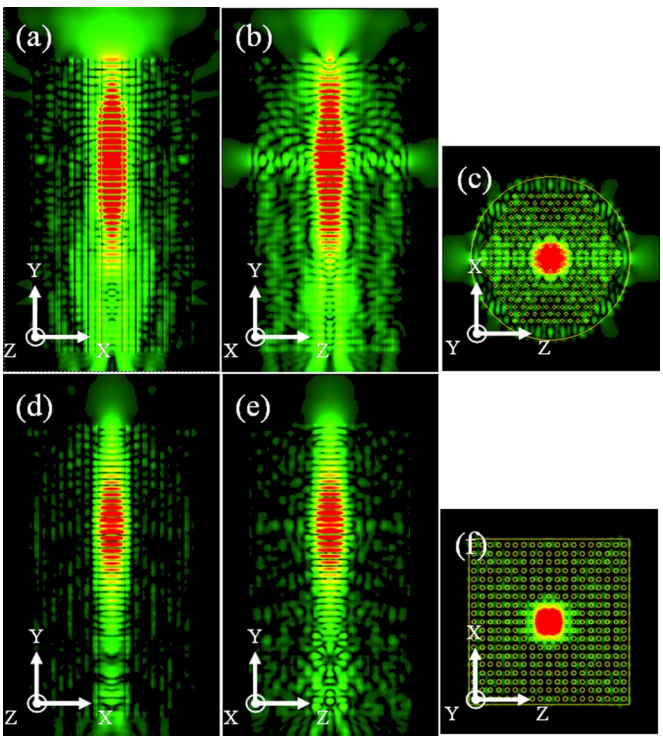

Fig. 11. Resonant frequency snapshot of the E_x-field for the triangular lattice quasi-3-D photonic crystal defect microcavity pillar in each plane (a) X-Y, (b) Y-Z, (c) X-Z, and for the square lattice quasi-3-D photonic crystal defect microcavity pillar in each plane (d) X-Y, (e) Y-Z, and (f) X-Z for the fundamental HE_{11} mode. The resonant wavelength is 950 nm in the triangular lattice quasi-3-D photonic crystal defect microcavity and 971 nm in the square lattice quasi-3-D photonic crystal defect microcavity.

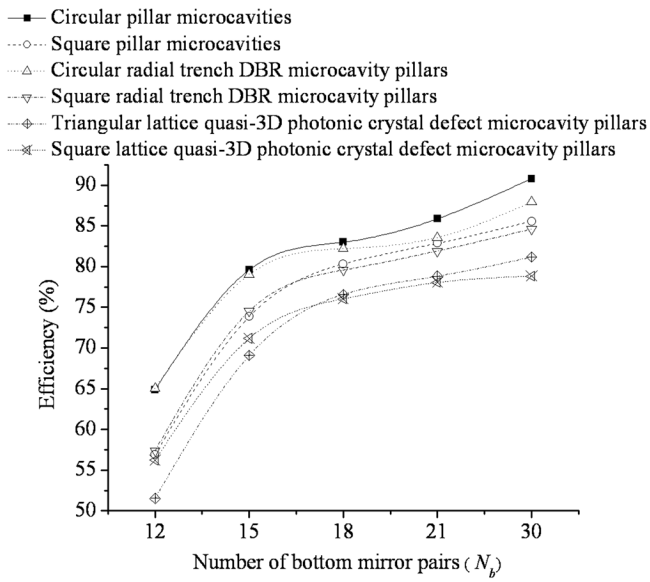

Fig. 12. Efficiency estimate from ratio of power emitted from top of device to the total emission using boxes labeled S in Fig. 2. This is plotted as a function of radius for a structure with fixed $N_t = 6$ top mirror pairs and N_b =12, 15, 18, 21, and 30 bottom pairs.

the pillar I_{tot} to total emission in an infinite slab of the bulk material I_{inf} should reflect the reduction in spontaneous lifetime induced in a dot and we can estimate the Purcell factor from

$$F_p \approx \frac{\tau_{\mathrm{inf}}}{\tau_{\mathrm{cav}}} \approx \frac{I_{\mathrm{tot}}}{I_{\mathrm{inf}}} \tag{4}$$

where τ_{cay} is spontaneous emission lifetime in the cavity, and τ_{inf} is spontaneous emission lifetime in the bulk material.

The total intensity is calculated in the same way as the efficiency results, summing the Poynting vector over a box around

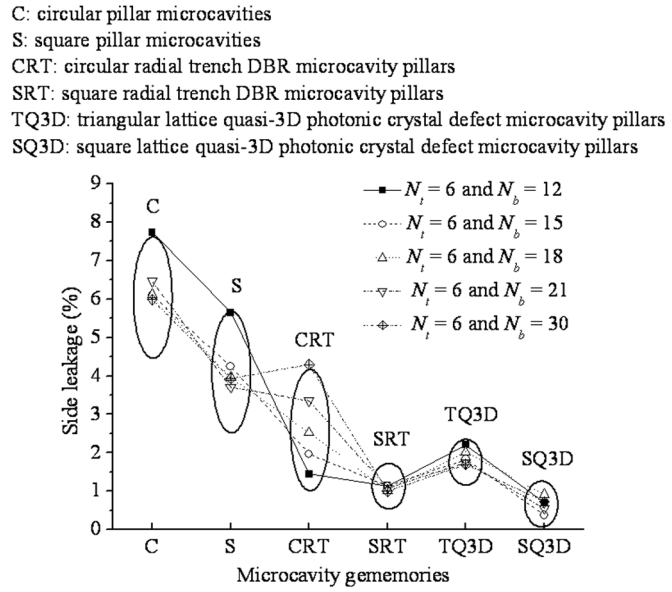

Fig. 13. Side leakage as a function of various cavity geometries with fixed $N_t = 6$ top mirror pairs and $N_b = 12$, 15, 18, 21, and 30 bottom mirror pairs.

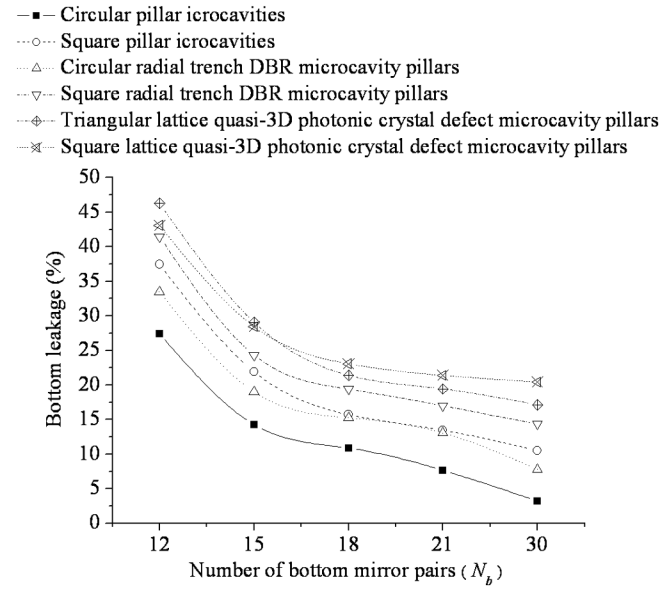

Fig. 14. Bottom leakage as a function of the number of mirror pairs for different type of micro-pillar microcavity geometries with fixed $N_t = 6$ top mirror pairs and $N_b = 12$, 15, 18, 21, and 30 bottom pairs.

the dipole with the microcavity (I_{tot}) and in a block of GaAs filling the simulation volume (I_{inf}).

Alternatively, a theoretical estimate of Purcell factor can be obtained from [2]

$$F_p \equiv \frac{3Q\left(\frac{\lambda_0}{n_h}\right)^3}{4\pi^2 V_{\text{eff}}} \tag{5}$$

where V_{eff} is the effective modal volume, Q is the cavity quality factor, and λ_0 is the cavity resonant wavelength.

We have used our FDTD results to estimate F_p for various pillar radii using a microcavity with $N_t = 6\,(15)$ mirror pairs on top and $N_b = 12\,(30)$ mirror pairs below and plot the results in Figs. 16 and 17. For the theoretical estimate, we use the FDTD measured Q-factor and estimate the cavity effective volume to lie between [19]

$$\frac{1}{4}\pi \cdot r^2 \cdot \frac{2\lambda_0}{n_h} < V_{\text{eff}} < \frac{1}{3}\pi \cdot r^2 \cdot \frac{2\lambda_0}{n_h} \tag{6}$$

where r is the pillar radius.

In the low-Q cavity, we see that the FDTD estimated Purcell factor increases as the cavity diameter decreases due primarily to the fall in cavity effective volume as the Q-factor remains reasonably constant down to the lowest diameters (Fig. 8). The FDTD results lie close to the theoretical bounds, although diverging at small diameters due to the field extending further into the air region, thus increasing the effective volume above

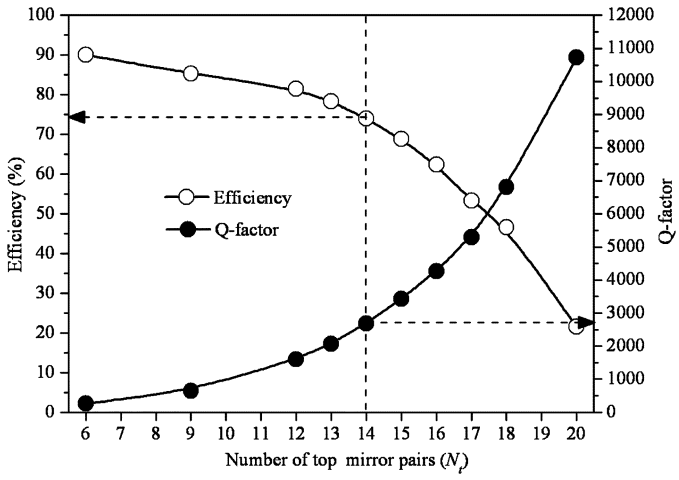

Fig. 15. Optimal values of the light extraction efficiency and the Q-factor plotted as a function of the number of top DBR pairs ($N_t = 6$ to 20 bottom pairs), each point being calculated for a fixed $N_b = 27$ bottom DBR mirror pairs.

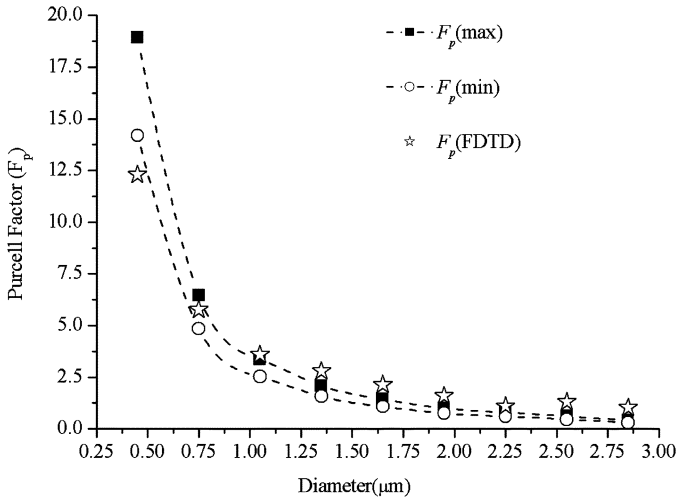

Fig. 16. FDTD theoretical estimates of Purcell factor are plotted for the fundamental mode of the micro-pillar microcavity with $N_t = 6$ top mirror pairs and $N_b = 12$ bottom mirror pairs as a function of each diameter. Dashed lines ($F_p(\max)$ and $F_p(\min)$) are calculated using (5) and (6).

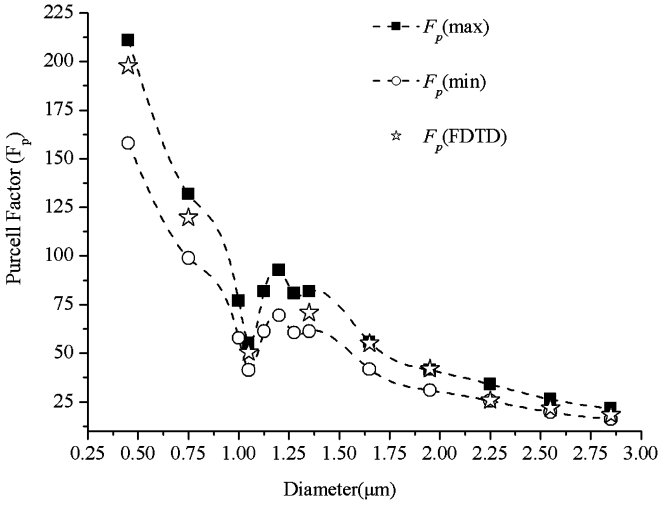

Fig. 17. FDTD theoretical estimates of Purcell factor are plotted for the fundamental mode of the micro-pillar microcavity with $N_t = 15$ top mirror pairs and $N_b = 30$ bottom mirror pairs as a function of each diameter. Dashed lines ($F_p(\max)$ and $F_p(\min)$) are calculated using (5) and (6).

the limit in (6). At small Purcell factors, we know (5) to be invalid as it should tend to unity in large pillars, which we see in the FDTD result. In the case of the high-Q pillars (Fig. 17), the Purcell factors increase as the diameter is reduced until 1-μm diameter where we see a dip. Then, the behavior becomes quite oscillatory reflecting the oscillations measured in the Q-factor (Fig. 8) eventually falling away as the Q-factor falls faster than the cavity modal volume. These Purcell factors are extremely high, much higher than experimentally measured. The maximum experimentally measured Purcell factors are in the region of 23 which was achieved at resonance [27]. This is primarily because we are treating a single dipole placed in the ideal position in the cavity. Most experiments use randomly located dots and do not achieve the theoretical Q-factors we are reporting here.

IV. Conclusion

This paper has primarily presented the 3-D FDTD design, simulation, and modeling of micro-pillar microcavity geometries which are suitable for the construction of high-efficiency single-photon sources. Where possible, we have successfully compared our numerical results with a simple TMM and an effective waveguide model (Section II).

We find that, for large-transverse-dimension circular or square pillars, the measured Q-factors are comparable with those of infinite dimension pillars. For high-Q cavities (e.g., $N_t = 15$ and $N_b = 30$), the Q-factors begin to drop at pillar dimensions of around 1 μm and show an oscillatory behavior due to transverse-mode mismatch between the various layers making up the cavity and mirrors. For low Q-factor pillar cavities (e.g., $N_t = 6$ and $N_b = 12$), we see little or no reduction of Q-factor with radius. This is primarily due to the rate of scattering loss always being small compared with the rate of loss from the cavity. Also, this suggests that, for efficient single-photon sources, it may be best to use lower Q cavities.

For the suppression of sidewall leakage, we have studied the microcavity geometries with quasi-3-D light confinement, such as the circular and square radial trench DBR microcavities and triangular lattice and square lattice photonic crystal defect microcavities. The quantitative results have confirmed that the side wall leakage is increasingly suppressed by the lateral confinement in these microcavity geometries. However, this suppression comes at the price of enhanced bottom leakage.

In this paper, we have also investigated the optimal design of DBR mirror pairs to balance a high-cavity Q-factor for strong enhancements of emission rates, while maximizing the collection efficiency for the spontaneous emission into the fundamental HE_{11} mode. In the case of the simple circular pillar microcavity, we have seen light extraction efficiency of more than 90% when increasing the number of bottom mirror pairs with fixed $N_t = 6$ top mirror pairs. However, the Q-factors are less than 400 due to the low-reflectivity top mirror. With fixed $N_b = 27$ bottom DBR mirror pairs and varying top mirror pairs from 6 to 20, we clearly see the tradeoff between collection efficiency and Q-factor (Fig. 15). We have since designed an experimental sample consisting of $N_t = 14$ and $N_b = 27$. This should give us a Q-factor $Q \sim 2700$ with fairly high-efficient vertical emission ($\eta \sim 75\%$). We estimate that the Purcell factor in a 1-μm-diameter cavity could be as high as 30. We have also estimated the Purcell factors in low-Q and high-Q cavities with varying diameter. We see very high Purcell factors in our high-Q cavities but expect that these will not be demonstrable in experiment due to limitations in the positioning of the QD and the extra scattering losses.

Acknowledgment

The authors would like to thank Dr. G. B. Ren for very fruitful discussions.

References

[1] H. Benisty, R. Stanley, and M. Mayer, "A method of source terms for dipole emission modification in modes of arbitrary planar structures," *J. Opt. Soc. Amer. A, Opt. Image Sci.*, vol. 15, pp. 1192–1201, 1998.

[2] E. M. Purcell, "Spontaneous emission probabilities at radio frequencies," *Phys. Rev.*, vol. 69, pp. 681–681, 1946.

[3] C. Santori, M. Pelton, G. Solomon, Y. Dale, and Y. Yamamoto, "Triggered single photons from a. quantum dot," *Phys. Rev. Lett.*, vol. 86, pp. 1502–1505, 2001.

[4] E. Moreau, I. Robert, J. M. Gérard, I. Abram, L. Manin, and V. Thierry-Mieg, "Single-mode solid-state single photon source based on isolated quantum dots in pillar microcavities," *Appl. Phys. Lett.*, vol. 79, pp. 2865–2867, 2001.

[5] M. Pelton, C. Santori, J. Vučković, B. Zhang, G. S. Solomon, J. Plant, and Y. Yamamoto, "Efficient source of single photons: A single quantum dot in a micropost microcavity," *Phys. Rev. Lett.*, vol. 89, pp. 233602–233602, 2002.

[6] C. Santori, D. Fattal, J. Vučković, G. S. Solomon, and Y. Yamamoto, "Indistinguishable photons from a single photon source," *Nature*, vol. 419, pp. 594–597, 2002.

[7] A. Beveratos, R. Brouri, T. Gacoin, A. Villing, J.-P. Poizat, and P. Grangier, "Single photon quantum cryptography," *Phys. Rev. Lett.*, vol. 89, pp. 187901–187901, 2002.

[8] J. G. Rarity, "Quantum communications and beyond," *Phil. Trans. R. Soc. Lond. A*, vol. 361, pp. 1507–1507, 2003.

[9] Y. Xu, J. Vuckovic, R. Lee, O. Painter, A. Scherer, and A. Yariv, "Finite-difference time-domain calculation of spontaneous emission lifetime in a microcavity," *J. Opt. Soc. Amer. B, Opt. Phys.*, vol. 16, pp. 465–474, 1999.

[10] G. S. Agarwal, "Quantum electrodynamics in the presence of dielectrics and conductors. IV. General theory for spontaneous emission in finite geometries," *Phys. Rev. A, Gen. Phys.*, vol. 12, pp. 1475–1497, 1975.

[11] A. Taflove and S. C. Hagness, *Computational Electrodynamics: The Finite-Difference Time-Domain Method*, 3rd ed. Boston, MA: Artech House, 2005.
[12] M. Pelton, J. Vuckovic, G. Solomon, A. Scherer, and Y. Yamamoto, "Three-dimensionally confined modes in micropost microcavities: Quality factors and Purcell factors," *IEEE J. Quantum Electron.*, vol. 38, no. 2, pp. 170–177, Feb. 2002.
[13] P. Yeh, *Optical Waves in Layered Media*. Chichester, U.K.: Wiley, 2005.
[14] A. Yariv, *Optical Electronics in Modern Communications*, 5th ed. New York: Wiley, 1997.
[15] J. M. Gérard, D. Barrier, J. Marzin, R. Kuszelewicz, L. Manin, E. Costard, V. T. Mieg, and T. Rivera, "Quantum boxes as active probes for photonic microstructures: The pillar microcavity case," *Appl. Phys. Lett.*, vol. 69, pp. 449–451, 1996.
[16] D. Ochoa, R. Houdre, M. Ilegems, H. Benisty, T. Krauss, and C. J. M. Smith, "Diffraction of cylindrical Bragg reflectors surrounding an in-plane semiconductor microcavity," *Phys. Rev. B, Condens. Matter*, vol. 61, pp. 4806–4812, 2000.
[17] E. Pavarini and L. C. Andreani, "Etched distributed Bragg reflectors as three-dimensional photonic crystals: Photonic bands and density of states," *Phys. Rev. E, Stat. Phys. Plasmas Fluids Relat. Interdiscip. Top.*, vol. 66, pp. 036602–036602, 2002.
[18] M. Ito, S. Iwamoto, and Y. Arakawa, "Enhancement of cavity-Q in a quasi-three- dimensional photonic crystal," *Jpn. J. Appl. Phys.*, vol. 43, pp. 1990–1994, 2004.
[19] L. C. Andreani, G. Panzarini, and J.-M. Gérard, "Strong-coupling regime for quantum boxes in pillar microcavities: Theory," *Phys. Rev. B, Condens. Matter*, vol. 60, pp. 13276–13279, 1999.
[20] T. Baba, T. Hamano, F. Koyama, and K. Iga, "Spontaneous emission factor of a microcavity DBR surface-emitting laser," *IEEE J. Quantum Electron.*, vol. 27, no. 5, pp. 1347–1358, May 1991.
[21] K. S. Yee, "Numerical solution of initial boundary value problems involving Maxwell's equations in isotropic media," *IEEE Trans. Antennas Propagat.*, vol. AP-14, no. 3, pp. 302–307, May 1966.
[22] S. G. Johnson and J. D. Joannopoulos, "Block-iterative frequency-domain methods for Maxwell's equations in a planewave basis," *Opt. Exp.*, vol. 8, pp. 173–190, 2001.
[23] G. Lecamp, P. Lalanne, J. P. Hugonin, and J.-M. Gerard, "Energy transfer through laterally confined Bragg mirrors and its impact on pillar microcavities," *IEEE J. Quantum Electron.*, vol. 41, no. 10, pp. 1323–1329, Oct. 2005.
[24] M. R. Watts, S. G. Johnson, H. A. Haus, and J. D. Joannopoulos, "Electromagnetic cavity with arbitrary Q and small modal volume without a complete photonic bandgap," *Opt. Lett.*, vol. 27, pp. 1785–1787, 2002.
[25] J. A. Timpson, S. Lam, D. Sanvitto, D. M. Whittaker, H. Vinck, A. Daraei, P. S. S. Guimaraes, M. S. Skolnick, A. M. Fox, C. Hu, Y.-L. D. Ho, R. Gibson, J. G. Rarity, A. Tahraoui, M. Hopkinson, P. W. Fry, S. Pellegrini, K. J. Gordon, R. E. Warburton, and G. S. Buller, "Single photon sources based upon single quantum dots in semiconductor microcavity pillars," *J. Mod. Opt.*, vol. 54, pp. 453–465, 2007.
[26] R. Sprik, B. A. v. Tiggelen, and A. Lagendijk, "Optical emission in periodic dielectrics," *Europhys. Lett.*, vol. 35, pp. 265–270, 1996.
[27] S. Varoutsis, S. Laurent, P. Kramper, A. Lemaître, I. Sagnes, I. Robert-Philip, and I. Abram, "Restoration of photon indistinguishability in the emission of a semiconductor quantum dot," *Phys. Rev. B, Condens. Matter*, vol. 72, pp. 041303–041303, 2005.

Ying-Lung Daniel Ho received the B.Sc. degree in electrical engineering from the National Taipei University of Technology, Taipei, Taiwan, R.O.C., in 1999. He is currently working toward the Ph.D. degree at the Photonics Research Group, Centre for Communications Research (CCR), Department of Electrical and Electronic Engineering, University of Bristol, Bristol, U.K.

His current research interests include finite-difference time-domain modeling and simulation of quantum optics in wavelength-scale structures and focused ion beam fabrication of micro/nano-optical devices, including single-photon sources.

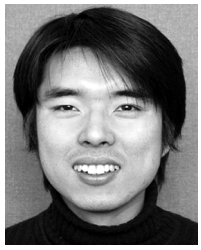

Tun Cao was born in Dalian, China, in 1979. He received the B.Eng. degree in electronic engineering and the B.Eng. degree in computer science from Dalian University of Technology, Dalian, China, in 2001 and 2002, respectively. He is currently working toward the Ph.D. degree with the Photonics Research Group, Ddepartment of Electrical and Electronic Engineering, University of Bristol, Briston, U.K.

His doctoral research is focused on finite-difference time-domain and finite-element analysis of photonic crystals. He has authored and coauthored 18 publications for national and international conferences.

Pavel S. Ivanov received the Dipl.-Ing. degree in electrical engineering (with honors) from Kharkiv National University of Radio Electronics, Kharkiv, Ukraine, in 1999, and the Ph.D. degree in optics and laser physics from Kharkiv National University, Kharkiv, Ukraine, in 2004.

In 2003–2004, he was a Teaching Assistant with Kharkiv National University of Radio Electronics and a Visiting Fellow with the University of Bristol, Bristol, U.K. During this time, and currently, as a Research Assistant at the University of Bristol, he has been involved in theoretical and experimental investigation of VCSELs incorporating two-dimensional photonic crystals.

Martin J. Cryan received the B.Eng. degree in electronic engineering from the University of Leeds, Leeds, U.K., in 1986, and the Ph.D. degree from the University of Bath, Bath, U.K., in 1995.

Prior to beginning his doctoral work, he worked in industry for five years as a Microwave Design Engineer. From 1994 to 1997, he was a Researcher with the University of Birmingham, Birmingham, U.K., where he worked on active integrated antennas. From 1997 to 1999, he was a European Union Training and Mobility of Researchers Research Fellow with the University of Perugia, Perugia, Italy, where he was involved with the design and simulation of quasi-optical multipliers using the lumped-element finite-difference time-domain (FDTD) method. From 2000 to 2002, he was a Research Associate with the University of Bristol, Briston, U.K., where he was involved with hybrid electromagnetic methods for electromagnetic compatibility problems in optical transceivers and FDTD analysis of photonic crystals. Since 2002, he has been a Lecturer with the Department of Electronic Engineering, University of Bristol. He has published 20 journal and 71 conference papers (seven invited) in the areas of fabrication, modeling, and measurement of photonic crystal based devices, RF-over-fiber, active integrated antennas, FDTD analysis, and monolithic microwave integrated circuit design.

Ian J. Craddock received the B.Eng. and Ph.D. degrees from the University of Bristol, Bristol, U.K., in 1992 and 1995, respectively.

He is a Reader with the Centre for CommunicationsResearch (CCR), University of Bristol. He has active research interests in finite-difference time-domain analysis, wideband antenna design, antenna arrays, MIMO, electromagnetic analysis, and microwave radar for breast cancer detection. He is part of the EU Framework 6 Antennas Network of Excellence, where he leads a work-package on antennas for GPR.

Chris J. Railton received the B.Sc. degree in physics from the University of London, London, U.K., in 1974, and the Ph.D. degree in electronic engineering from the University of Bath, Bath, U.K., in 1988.

During 1974–1984, he worked with the Scientific Civil Service on various research and development projects in the areas of communications, signal processing, and electromagnetic compatibility (EMC). From 1984 to 1987, he was with the University of Bath, working on the mathematical modeling of boxed microstrip circuits. Currently, he is the Head of Computational Electromagnetics Group, Centre for Communications Research, University of Bristol, Bristol, U.K., where he is engaged in the development of new algorithms for electromagnetic analysis and their application to the design of monolithic microwave integrated circuits, planar and conformal antennas, microwave and RF heating systems, EMC, high-speed interconnects, and optical waveguide components.

John G. Rarity received the B.Sc. (hons.) degree in physics from the University of Sheffield, Sheffield, U.K., in 1975, the M.Sc. degree in biophysics and bioengineering from Chelsea College, London, U.K., in 1976, and the Ph.D. degree from the Royal Military College of Science, Shrivenham, (now Cranfield), U.K., in 1984.

He joined the Royal Signals and Radar Establishment (now QinetiQ) in 1982. In the late 1980s, he began to study quantum interference effects, particularly counterintuitive effects involving two particles known as entanglement. The discovery and his subsequent development of quantum cryptography, a way of distributing keys over optical channels in absolute security using single-photon interference effects, was the first application in the emerging field of quantum information science. He has subsequently coordinated the European Union (EU) consortia EQCSPOT (framework 4) and RAMBOQ (framework 5) developing quantum cryptography and optical quantum computing and is presently active in several EU Framework 6 projects. He joined the University of Bristol, Bristol, U.K., in January 2003 as a Professor of Optical Communications. His work is currently focused on developing low-cost quantum cryptography systems and multiphoton entanglement experiments aiming to build scalable quantum logic devices.

Dr. Rarity was the recipient of the Thomas Young Medal from the Institute of Physics in 1995.